ADVANCED MATERIALS
www.advmat.de

Control of Charge-Spin Interconversion in van der Waals Heterostructures with Chiral Charge Density Waves

*Zhendong Chi, Seungjun Lee, Haozhe Yang, Eoin Dolan, C. K. Safeer, Josep Ingla-Aynés, Franz Herling, Nerea Ontoso, Beatriz Martín-García, Marco Gobbi, Tony Low, Luis E. Hueso, and Fèlix Casanova**

A charge density wave (CDW) represents an exotic state in which electrons are arranged in a long-range ordered pattern in low-dimensional materials. Although the understanding of the fundamental character of CDW is enriched after extensive studies, its practical application remains limited. Here, an unprecedented demonstration of a tunable charge-spin interconversion (CSI) in graphene/1T-TaS_2 van der Waals heterostructures is shown by manipulating the distinct CDW phases in 1T-TaS_2. Whereas CSI from spins polarized in all three directions is observed in the heterostructure when the CDW phase does not show commensurability, the output of one of the components disappears, and the other two are enhanced when the CDW phase becomes commensurate. The experimental observation is supported by first-principles calculations, which evidence that chiral CDW multidomains in the heterostructure are at the origin of the switching of CSI. The results uncover a new approach for on-demand CSI in low-dimensional systems, paving the way for advanced spin-orbitronic devices.

1. Introduction

Efficient and controllable charge-spin interconversion (CSI) obtained in materials with strong spin-orbit coupling is crucial for novel spin-orbitronic applications such as non-volatile memory[1] and logic devices.[2,3] Conventional CSI effects include the spin Hall effect (SHE) in bulk materials[4] and the Rashba–Edelstein effect (REE) in 2D systems with broken inversion symmetry.[5] By these mechanisms, a spin current (j_s), in the former, or a spin density (n_s), in the latter, are generated by a charge current (j_c). Both effects obey reciprocity, leading to inverse effects with the same efficiency.[6,7] In conventional materials with high symmetry, the directions of j_c and spin polarization (S) are perpendicular. Although large CSI values have been demonstrated in various systems,[8–11] controlling the CSI efficiency to design advanced multifunctional devices remains challenging.

Van der Waals materials, which have high electronic/structural tunability, provide a versatile platform for investigating novel spin-orbitronic phenomena.[12] Graphene (Gr) is an excellent van der Waals material for transferring spin current,[13] but its weak spin-orbit coupling limits the generation of CSI. To overcome this issue, Gr can be combined with transition metal dichalcogenides (TMDCs) to form van der Waals heterostructures,[14,15] in which the strong spin-orbit coupling in the TMDC is imprinted onto Gr by proximity effect. Large CSI in Gr/TMDC heterostructures has been predicted[16–19] and subsequently confirmed in experiments.[20–23] An unconventional CSI, with j_c collinear to S, has been observed in some

Z. Chi, H. Yang, E. Dolan, C. K. Safeer, J. Ingla-Aynés, F. Herling, N. Ontoso, B. Martín-García, L. E. Hueso, F. Casanova
CIC nanoGUNE BRTA
Donostia-San Sebastián 20018, Basque Country, Spain
E-mail: f.casanova@nanogune.eu

S. Lee, T. Low
Department of Electrical and Computer Engineering
University of Minnesota
Minneapolis, MN 55455, USA

C. K. Safeer
Department of Physics
Clarendon Laboratory
University of Oxford
Oxford OX1 3PU, UK

B. Martín-García, M. Gobbi, L. E. Hueso, F. Casanova
IKERBASQUE
Basque Foundation for Science
Bilbao 48009, Basque Country, Spain

M. Gobbi
Centro de Física de Materiales (CSIC-EHU/UPV) and Materials Physics Center (MPC)
Donostia-San Sebastián 20018, Basque Country, Spain

T. Low
Department of Physics
University of Minnesota
Minneapolis, MN 55455, USA

The ORCID identification number(s) for the author(s) of this article can be found under https://doi.org/10.1002/adma.202310768

DOI: 10.1002/adma.202310768

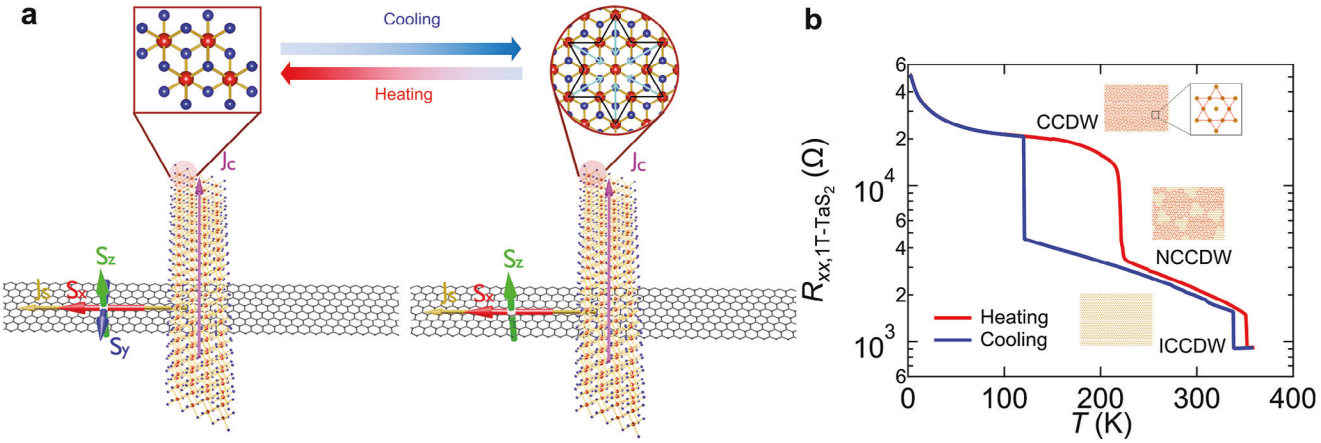

Figure 1. Graphene/1T-TaS_2 crystal structure and the CSI. a) Schematic illustrations of CSI in graphene/1T-TaS_2 heterostructures in different 1T-TaS_2 phases. The spin polarization of the spin current (j_s, yellow arrow) along the *x*-, *y*-, and *z*-axes are labeled by red, blue, and green arrows. Top panel: top views of 1T-TaS_2 crystal structure in the normal (left) and CDW (right) states. The black lines in the sketch of the CDW state display the structure of the stars of David in 1T-TaS_2. The cyan arrows illustrate the distortion of the surrounding Ta atoms toward the central Ta atom. The middle arrows represent cooling (blue) and heating (red) cases. b) Temperature (*T*) dependent resistance of the 60-nm-thick 1T-TaS_2 nanocrystal ($R_{xx,1T-TaS_2}$) in Device 1 while cooling (blue) and heating (red). Insets: formation of the stars of David in different CDW phases.

Gr/TMDC systems[24–28] and attributed to the broken mirror symmetries at the twisted interface.[29–32] A remarkable characteristic of Gr/TMDC heterostructures is their tunable CSI efficiency by using a gate voltage to shift the Fermi level in Gr.[21,22] However, controlling the CSI using the degrees of freedom in the TMDC counterpart has not yet been achieved.

The charge density wave (CDW), a long-range ordered state of electrons observed in low-dimensional materials, including TMDC, exhibits a thermally activated modulation. Beyond its wide exploration for the fundamental connections with some correlated states of matter, such as unconventional superconductivity,[33] its relationship with functional phenomena might be a promising direction. Here, we explore 1T-TaS_2, a TMDC featuring helical CDW phases with various degrees of commensurability,[34–36] as an ideal platform for controlling CSI. By spin precession experiments, we confirm the CSI with the spins polarized in the three directions predicted in the twisted Gr/1T-TaS_2 heterostructures.[32] Furthermore, we observe the ON and OFF of the unconventional CSI component by tuning the commensurability of the CDW phase (**Figure 1a**). Our first-principles calculations based on density functional theory (DFT) reveal that the disappearance of the unconventional CSI arises from the presence of chiral CDW multidomains in the commensurate phase in the heterostructures, where the sign of the CSI is locked to the chirality. The rich interplay between proximity, commensurability, and chirality of the CDW in the Gr/1T-TaS_2 van der Waals heterostructures opens the path to tailor a plethora of spin-based phenomena in low-dimensional systems.

2. Results and Discussion

2.1. Gr/1T-TaS_2 Heterostructure CSI Devices

1T-TaS_2 undergoes a reversible incommensurate CDW (ICCDW) to nearly commensurate CDW (NCCDW) phase transition and a NCCDW to commensurate CDW (CCDW) phase transition by modulating the temperature,[34] displaying a resistance hysteresis loop during a temperature sweep (Figure 1b). In the CCDW phase, 1T-TaS_2 is filled with a star-of-David-like CDW lattice distortion from the normal state (Figure 1a), exhibiting an insulating-like behavior. However, domains containing several tens of CDW stars of David exist in the NCCDW phase while slight Ta-atom-position-shifts are observed in the ICCDW phase (see insets of Figure 1b). The electrical transport in these two phases is thus limited by the normal metallic state.[37] This statement is also supported by a recent scanning tunnel microscope (STM) study, where the conductance across the domain walls of distinct insulating CCDW domains in 1T-TaS_2 is observed to be significantly higher than that within the CCDW domains.[38] Note that, although the band structures of 1T-TaS_2 in the ICCDW and NCCDW phases have been observed to show significant differences,[39,40] the case should be different in Gr/1T-TaS_2 heterostructures due to the charge transfer/carrier doping from Gr to the 1T-TaS_2 layer. The nature of the interfacial environment and transferred spin-orbit coupling from 1T-TaS_2 to Gr are contingent upon the CDW phase of 1T-TaS_2.[32] Therefore, tunable CSI is expected in Gr/1T-TaS_2 heterostructures.

To thoroughly investigate the CSI in Gr/1T-TaS_2 heterostructures, we fabricated three different devices (see Experimental Section and Notes S1–S3, Supporting Information, for details on device fabrication and characterization). **Figure 2a** illustrates the measurement configuration of CSI. The device consists of a Gr/1T-TaS_2 Hall bar heterostructure, ferromagnetic (FM) electrodes, and non-magnetic (NM) electrodes. The FM electrodes are designed as elongated nanowires to obtain a magnetic easy axis along the *y*-axis. In our measurement, a dc charge current (I_{dc}) is applied across the 1T-TaS_2 layer. In the presence of CSI in the heterostructure, the charge current is converted into a spin current which diffuses in Gr along the *x*-axis while keeping its spin polarization (S_x, S_y, and S_z shown in Figure 2a). Such spin current generates a non-local voltage (V_{NL}) at the FM/Gr interface, which we detect between the FM and NM electrodes on Gr. The non-local CSI resistance is defined as $R_{NL} = V_{NL}/I_{dc}$. To disentangle the CSI components induced by different spin

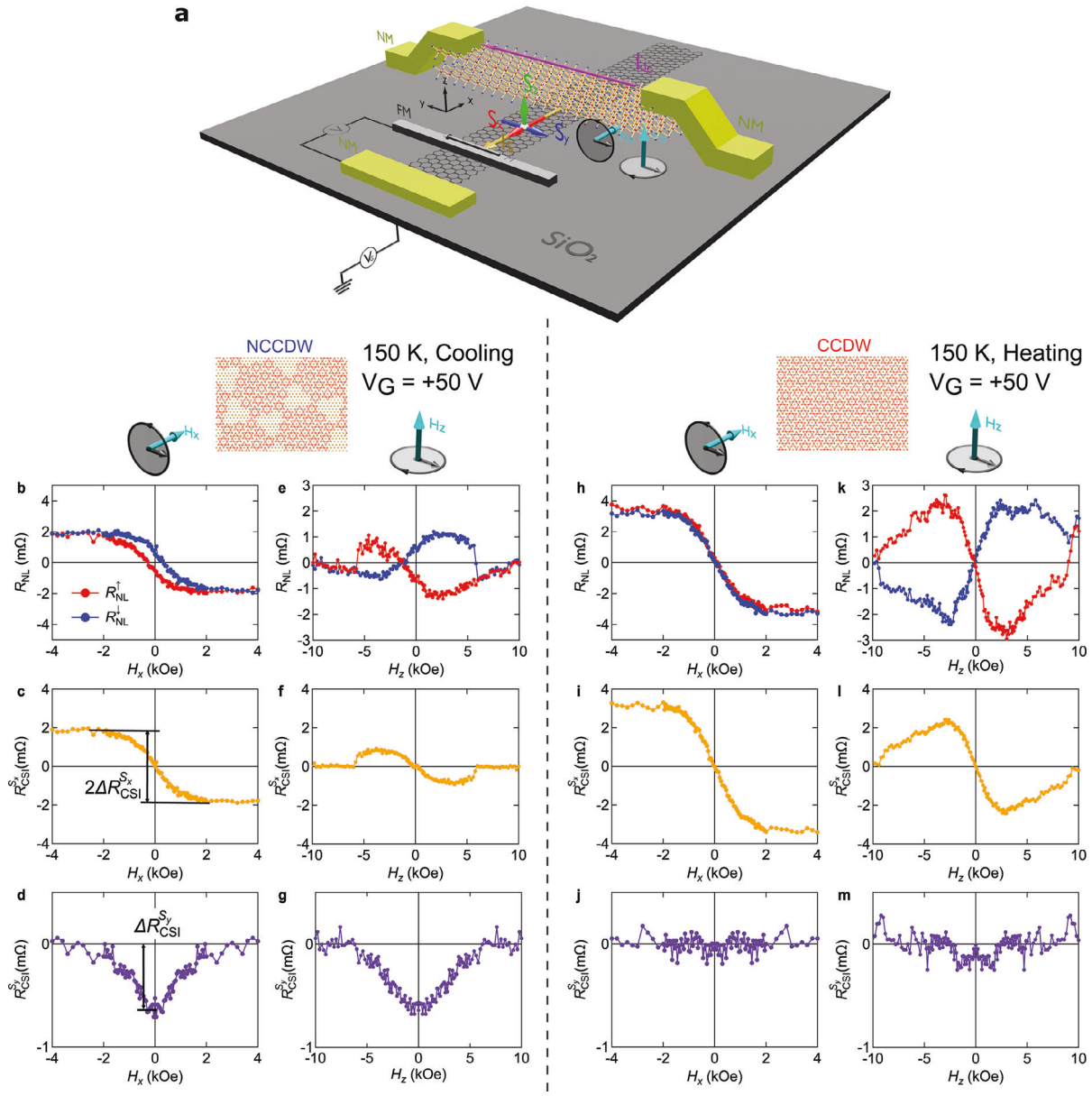

Figure 2. CSI characterization of Gr/1T-TaS_2 heterostructure Device 1 with different 1T-TaS_2 CDW phases. a) Schematic illustration of the CSI device. The device consists of a Gr/1T-TaS_2 heterostructure Hall bar cross junction, ferromagnetic (FM) nanowire electrodes (grey), and non-magnetic (NM) electrodes (light green). The bottom-right sketches illustrate the Hanle precession of the spin current under magnetic fields applied along the x (H_x) and z (H_z) axes. The gate voltage (V_G) is applied through the SiO_2 layer of the substrate. b) Non-local CSI resistance (R_{NL}) measured as a function of H_x with the NCCDW phase of 1T-TaS_2. The initial magnetization directions of the FM electrode are set along the $+y$ ($R^{\uparrow}_{NL}$, red line) and $-y$ directions ($R^{\downarrow}_{NL}$, blue line). c) H_x-dependent CSI component induced by spin current with spin polarization along the x-axis ($R^{S_x}_{CSI}$) extracted by averaging the two curves in (b). The amplitude of $R^{S_x}_{CSI}$ is labeled as $\Delta R^{S_x}_{CSI}$. d) H_x-dependent CSI component induced by spin current with spin polarization along the y-axis ($R^{S_y}_{CSI}$) obtained by symmetrizing the half of the difference of the two curves in (b). The amplitude of $R^{S_y}_{CSI}$ is labeled as $\Delta R^{S_y}_{CSI}$. e) $R^{\uparrow}_{NL}$ (red line) and $R^{\downarrow}_{NL}$ (blue line) measured as a function of H_z with the NCCDW phase of 1T-TaS_2. The sudden jump of the two curves at $|H_z| \approx 5$ kOe is attributed to a magnetization switching of the FM electrode but does not affect the spin precession feature of the curves. f) H_z-dependent $R^{S_x}_{CSI}$ obtained by antisymmetrizing the half of the difference of the two curves in (e). g) H_z-dependent $R^{S_y}_{CSI}$ extracted by symmetrizing half of the difference between the two curves in (e). h) $R^{\uparrow}_{NL}$ (red line) and $R^{\downarrow}_{NL}$ (blue line) measured as a function of H_x with the CCDW phase of 1T-TaS_2. i) H_x-dependent $R^{S_x}_{CSI}$ acquired by averaging the two curves in (h). j) H_x-dependent $R^{S_y}_{CSI}$ obtained by symmetrizing half of the difference of the two curves in (h). k) $R^{\uparrow}_{NL}$ (red line) and $R^{\downarrow}_{NL}$ (blue line) measured as a function of H_z with the CCDW phase of 1T-TaS_2. l) H_z-dependent $R^{S_x}_{CSI}$ acquired by antisymmetrizing the half of the difference of the two curves in (k). m) H_z-dependent $R^{S_y}_{CSI}$ obtained by symmetrizing half of the difference of the two curves in (k). A constant baseline of 1.9, 2.9, 6.8, and 8.6 mΩ has been subtracted from the curves in (b), (e), (h), and (k), respectively. All data was collected at 150 K with a gate voltage $V_G = +50$ V.

polarizations ($R_{CSI}^{S_x}$, $R_{CSI}^{S_y}$, and $R_{CSI}^{S_z}$), we measure R_{NL} by sweeping an external magnetic field along the *x*- (H_x) and *z*-axes (H_z), inducing Hanle precession of the spin current[20] (see Experimental Section for details). The magnetic properties of the FM electrodes and the spin transport characteristics of the pristine Gr and Gr/1T-TaS_2 heterostructure have been characterized individually in the same device using a non-local spin valve and Hanle precession measurements (see Note S5, Supporting Information, for details).[41] An electrical gate voltage (V_G) was applied to Gr to tune its Fermi level.

2.2. CDW Phase Dependence of CSI

Figure 2 illustrates the dependence of the CDW phase on the CSI characterization in Device 1 (bilayer Gr/60-nm-thick 1T-TaS_2) at $V_G = +50$ V. All the measurements were performed at 150 K, where either the NCCDW or the CCDW phase of 1T-TaS_2 can be stabilized by cooling or heating (Figure 1b), while the Gr properties remain constant. Figure 2b displays the H_x-dependent R_{NL} at the NCCDW phase. The red ($R_{NL}^{\uparrow}$) and blue ($R_{NL}^{\downarrow}$) curves were measured with the magnetization $\boldsymbol{M}$ of the FM electrode (Figure 2a) initially set along the $+y$ and $-y$ directions. To extract the different CSI components, we define $R_{NL}^{avg}(H_x) = (R_{NL}^{\uparrow} + R_{NL}^{\downarrow})/2$ and $R_{NL}^{diff}(H_x) = (R_{NL}^{\uparrow} - R_{NL}^{\downarrow})/2$. This average corresponds to the CSI component of the spins polarized along the *x*-axis ($R_{CSI}^{S_x}(H_x) \equiv R_{NL}^{avg}(H_x)$) and the difference includes both the CSI components of the spins polarized along the *y*- ($R_{CSI}^{S_y}$) and *z*-axes ($R_{CSI}^{S_z}$). $R_{CSI}^{S_y}$ and $R_{CSI}^{S_z}$ can be further distinguished by symmetrizing and antisymmetrizing $R_{NL}^{diff}(H_x)$, respectively (see Experimental Section for details).

The extracted $R_{CSI}^{S_x}$ is presented as a function of H_x in Figure 2c, revealing an *S*-shaped curve. The value of $R_{CSI}^{S_x}$ increases with increasing $|H_x|$ and reaches a maximum of 1.9 mΩ at $|H_x| \approx 2$ kOe, where $\boldsymbol{M}$ is fully saturated along the *x*-axis. Figure 2d illustrates the H_x-dependence of $R_{CSI}^{S_y}$, which has a maximum of 0.7 mΩ when H_x is zero and decreases as H_x increases until it vanishes at $|H_x| \approx 2$ kOe. This CSI component is confirmed by measuring R_{NL} as a function of H_y, which shows a squared hysteresis loop (see Note S7, Supporting Information, for details). $R_{CSI}^{S_z}$ is not shown, as it is below the noise level. Note that the *S*-shaped curve of $R_{CSI}^{S_x}$ with H_x could also be a spurious effect originating from the ordinary Hall effect in Gr induced by the stray field of the FM electrode.[42] To confirm the spin transport origin of the signal, that is, CSI, R_{NL} was measured by sweeping H_z to obtain the spin precession in the *x*–*y* plane. Figure 2e displays $R_{NL}^{\uparrow}$ and $R_{NL}^{\downarrow}$ as a function of H_z. In this case, $R_{CSI}^{S_x}$ and $R_{CSI}^{S_y}$ are extracted by defining $R_{NL}^{diff}(H_z) = (R_{NL}^{\uparrow} - R_{NL}^{\downarrow})/2$ and taking the antisymmetric and symmetric part, respectively (see Experimental Section). Figure 2f shows that $R_{CSI}^{S_x}$ exhibits a clear antisymmetric Hanle precession feature versus H_z, reaching a maximum of 0.9 mΩ at $H_z \approx 3$ kOe. $R_{CSI}^{S_y}$ is plotted as a function of H_z in Figure 2g, showing a maximum of 0.7 mΩ when H_z is zero and decreasing with increasing H_z. The maxima of $R_{CSI}^{S_y}$ in both H_x- and H_z-dependent measurements are in good agreement. These results provide unequivocal proof that the CSI signals in Figure 2b,e are induced by the CSI components of spin currents polarized along the *x*- and *y*-axes. We determine the amplitude of $R_{CSI}^{S_x}$ and $R_{CSI}^{S_y}$ using, respectively, the step height in Figure 2c ($\Delta R_{CSI}^{S_x} \equiv (R_{CSI}^{S_x}(H_x = 2\text{ kOe}) - R_{CSI}^{S_x}(H_x = -2\text{ kOe}))/2$) and the maximum value in Figure 2d ($\Delta R_{CSI}^{S_y} \equiv |R_{CSI}^{S_y}(H_x = 0)|$).

Similar measurements were conducted after driving the NCCDW-CCDW phase transition in 1T-TaS_2 and stabilizing the CCDW phase at 150 K. The resulting R_{NL} and the corresponding $R_{CSI}^{S_x}$ and $R_{CSI}^{S_y}$ are plotted as a function of H_x (Figure 2h–j) and H_z (Figure 2k–m). The *S*-shaped curve (antisymmetric Hanle precession) of $R_{CSI}^{S_x}$ as a function of H_x (H_z) indicates that the CSI component induced by *x*-polarized spin current persists in the CCDW phase. $\Delta R_{CSI}^{S_x}$ increases by approximately a factor of two after the phase transition. Interestingly, regardless of whether the magnetic field is applied along the *x*- or *z*-axis, $R_{CSI}^{S_y}$ is nearly zero. This result evidences that the unconventional CSI is switched off in our heterostructure when 1T-TaS_2 is in the CCDW phase.

To investigate whether the disappearance of the unconventional CSI in Gr/1T-TaS_2 heterostructure during the phase transition is reproducible, we repeated the experiment in another device (Device 2, monolayer Gr/100-nm-thick 1T-TaS_2). $R_{CSI}^{S_x}$, $R_{CSI}^{S_y}$, and $R_{CSI}^{S_z}$ obtained with the NCCDW and CCDW phases are plotted as a function of H_x in **Figure 3**a,b, respectively. We find that $R_{CSI}^{S_y}$ disappears again after the phase transition while $R_{CSI}^{S_x}$ exists regardless of the CDW phase, confirming the previous observation.

Interestingly, although $R_{CSI}^{S_z}$ in Device 1 is lower than the noise level, we clearly observe $R_{CSI}^{S_z}$ in Device 2 when 1T-TaS_2 is in either the NCCDW or the CCDW phase, as shown by the clear antisymmetric Hanle precession cyan curves in Figure 3a,b, respectively. This CSI component is also detected in another device (Device 3, few-layer Gr/22-nm-thick 1T-TaS_2), indicating that the number of Gr layers is not the reason for observing $R_{CSI}^{S_z}$. We note that the spin injection efficiency of the FM electrodes, estimated from non-local spin valve measurements, is much lower in Device 1 than in Devices 2 and 3 (see Note S5, Supporting Information). Compared to the relatively large $\Delta R_{CSI}^{S_x}$ and $\Delta R_{CSI}^{S_y}$, especially when 1T-TaS_2 is in the NCCDW phase (Figure 3a), the lower spin injection efficiency in Device 1 prevents the detection of the small $R_{CSI}^{S_z}$ component.

We also investigated CSI in Device 3 when 1T-TaS_2 is in the ICCDW phase (see Note S8, Supporting Information, for details). All three CSI components are observed at 360 K. As discussed above, the transport in 1T-TaS_2 is principally governed by the normal state, both in the NCCDW and ICCDW phases. Conversely, in the CCDW phase, the CDW state predominates, thereby instigating insulating-like behavior. These results suggest that the phase-dependent switching of the unconventional CSI ($R_{CSI}^{S_y}$) is linked to the change in the transport regime (that is, commensurability) of 1T-TaS_2.

2.3. Temperature and Gate Voltage Dependencies of CSI

After confirming an omnidirectional CSI and a phase-transition-driven switchable unconventional CSI, we studied the temperature (T) and gate voltage (V_G) dependencies of CSI. $\Delta R_{CSI}^{S_x}$ and

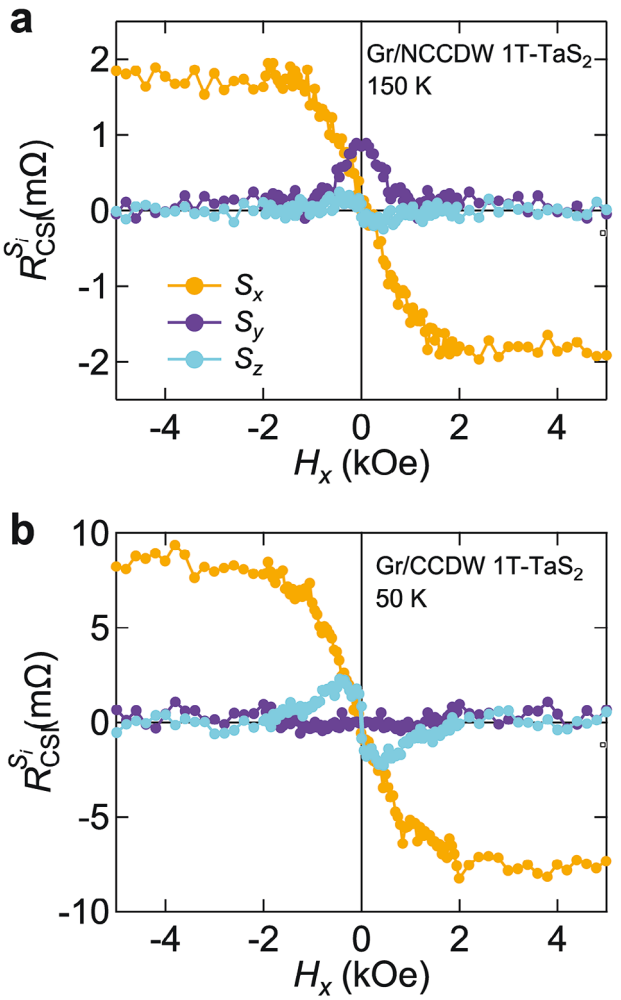

Figure 3. Spin-polarization direction-dependent CSI in Device 2. Different components of the CSI ($R^{S_i}_{CSI}$) extracted from the non-local CSI resistance measured as a function of H_x in Device 2. $R^{S_i}_{CSI}$ in Gr/NCCDW 1T-TaS_2 heterostructure at 150 K and in Gr/CCDW 1T-TaS_2 heterostructure at 50 K are displayed in (a) and (b), respectively. $R^{S_i}_{CSI}$ originating from spin currents with spin polarization along the x ($R^{S_x}_{CSI}$), y ($R^{S_y}_{CSI}$), and z ($R^{S_z}_{CSI}$) axes are plotted as orange, purple, and cyan curves, respectively. All the measurements were performed without applying a gate voltage. See Note S6, Supporting Information, for the raw data.

$\Delta R^{S_y}_{CSI}$ extracted from Device 1 are plotted as a function of T in **Figure** 4a. We observe that both $\Delta R^{S_x}_{CSI}$ and $\Delta R^{S_y}_{CSI}$ increase as T decreases, regardless of the phase of 1T-TaS_2. Furthermore, $\Delta R^{S_x}_{CSI}$ exhibits a phase-related hysteresis loop with T, which is consistent with the resistance hysteresis loop of 1T-TaS_2 (Figure 1b). This agreement indicates that the resistance of 1T-TaS_2 influences the CSI output in Gr/1T-TaS_2 heterostructures.

Figure 4b illustrates $\Delta R^{S_x}_{CSI}$ and $\Delta R^{S_y}_{CSI}$ extracted from Device 1 at 150 K as a function of V_G. All the CSI components follow a similar trend with respect to V_G: their magnitudes reach a minimum when $V_G = -40$ V, that is, the charge neutrality point of the Gr/1T-TaS_2 heterostructure (Figure 4c), and increases as V_G increases from −40 V. The values reach saturation after V_G is increased up to +40 V. This behavior differs from that observed in the resistance of Gr/1T-TaS_2 heterostructure (Figure 4c). To understand the observed V_G dependence, we measured the charge and spin transport properties of Device 1 at 150 K with different V_G. The resistance of 1T-TaS_2 exhibits negligible changes with V_G (Figure S4b,c in Note S4, Supporting Information). In contrast, the spin injection efficiency, given by the non-local spin valve signal shown in Figure 4d (see details on the measurement in Note S5, Supporting Information), shows a similar dependence on V_G as the CSI output. Therefore, we suggest that the tuning of the CSI output by the gate voltage can be primarily attributed to the gate tuning of the spin injection efficiency at the Gr/FM electrode interface. Similar T and V_G dependencies of CSI are obtained in Device 3 (see Note S8, Supporting Information).

Table 1. Spin Hall conductivity in bulk 1T-TaS_2 and the graphene/1T-TaS_2 heterostructure calculated in the CCDW and normal phases of 1T-TaS_2.

		σ^x_{xy}	σ^y_{xy}	σ^z_{xy}	σ^x_{zy}	σ^y_{zy}	σ^z_{zy}
1T-TaS_2	Normal	6.5	6.5	59.6	22	–	–
	CDW	9	8	24	15	3	1
Gr/1T-TaS_2	Normal	6	6	53	–	–	–
	CDW	15	20	18	–	–	–

The spin Hall conductivity is represented by σ^k_{ij}, where i, j, and k represent the spin current, charge current, and spin polarization directions, respectively. Since σ^k_{ij} is very sensitive to the crystallographic orientation, each number indicates the maximum values of σ^k_{ij} for any possible crystal orientations. All units are in $((\hbar/e)$S/cm).

2.4. The Origin of the CSI

The observed CSI in the Gr/1T-TaS_2 heterostructures can have different origins: the SHE inherent to the bulk 1T-TaS_2, the interfacial SHE arising from the spin-orbit proximity, and the REE generated by the broken inversion symmetry at the interface. To gain insight into the underlying mechanisms of tunable CSI driven by the commensurability of the CDW phase, we perform first-principles calculations based on DFT (see Experimental Section) to analyze the CSI of bulk 1T-TaS_2 and of the Gr/1T-TaS_2 van der Waals heterostructure in the normal and the CCDW states of 1T-TaS_2.

We investigate first the SHE of bulk 1T-TaS_2 by calculating the spin Hall conductivity tensor σ^k_{ij}, where i, j, and k represent the directions of j_s, j_c, and S, respectively. In our measurement, the charge current is along the y-axis, whereas the spin current direction in the bulk 1T-TaS_2 can be either along the x-axis ($j_{s,x}$) or along the z-axis ($j_{s,z}$) due to the absorption from Gr, as seen in metallic systems.[41] **Table** 1 summarizes the calculated σ^k_{ij} values of possible elements in our measurement configuration, determined by the spin Berry curvature component Ω^k_{ij} (see Note S9, Supporting Information, for details). On the one hand, for $j_{s,x}$, σ^z_{xy} is much larger than σ^x_{xy} and σ^y_{xy} in the normal state. These values suggest the $R^{S_z}_{CSI}$ would be the largest CSI component detected in the NCCDW or ICCDW phase of 1T-TaS_2. However, this prediction contradicts our experimental results, leading us to exclude the possibility of CSI originating from the SHE of bulk 1T-TaS_2 induced by $j_{s,x}$. On the other hand, for $j_{s,z}$, σ^y_{zy}

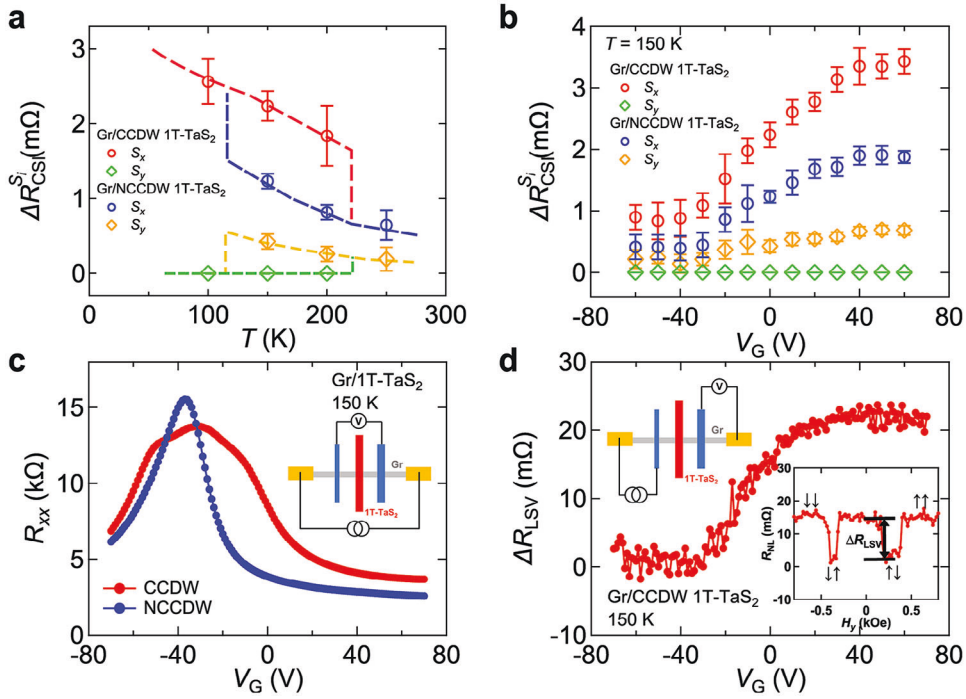

Figure 4. Temperature (T) and gate voltage (V_G) dependencies of CSI in Device 1. a) T dependence of $\Delta R^{S_i}_{CSI}$ measured without adding gate voltage. $\Delta R^{S_x}_{CSI}$ in the heterostructure in the NCCDW (CCDW) phase of 1T-TaS_2 are displayed by red (blue) circles. $\Delta R^{S_y}_{CSI}$ in the heterostructure in the NCCDW phase of 1T-TaS_2 is shown by orange diamonds. The vanished $\Delta R^{S_y}_{CSI}$ in the heterostructure in the CCDW phase of 1T-TaS2 is represented by the green diamonds, with all the values equal to zero. The dashed curves are a guide to the eye for the hysteresis loops observed in $\Delta R^{S_i}_{CSI}$. b) V_G dependence of $\Delta R^{S_i}_{CSI}$ measured at $T = 150$ K. c) V_G dependence of the longitudinal resistance of the Gr/1T-TaS_2 heterostructure (R_{xx}) when 1T-TaS_2 is at the CCDW (red circles) and NCCDW (blue circles) phases. Inset: a sketch of the measurement configuration. d) V_G dependence of the non-local spin valve signal (ΔR_{LSV}) measured across the Gr/CCDW 1T-TaS_2 heterostructure at 150 K. Insets: Sketch of the measurement configuration (left) and the non-local resistance of the spin valve (R_{NL}) measured with $V_G = 0$ V (right). The definition of ΔR_{LSV} is labeled. Error bars are calculated using the standard deviation associated with the statistical average of $R^{S_i}_{CSI}$ in both the positive and negative magnetic field ranges.

and σ^z_{zy} are strictly zero (due to symmetry constrain)[43] or negligible for the normal and CCDW states, respectively, indicating that the conventional SHE (σ^x_{zy}) in bulk 1T-TaS_2 is the only bulk 1T-TaS_2-originated component that can contribute to the observed $R^{S_x}_{CSI}$.

Next, we investigate the interfacial SHE of the Gr/1T-TaS_2 heterostructure with a twisted angle of 13.9°. The calculated σ^k_{ij} values are summarized in Table 1 (see Note S9, Supporting Information, for details). By nature of the interfacial effect, the direction of the spin current is constrained to the x-axis. In the calculated spin Berry curvature, it becomes evident that the Dirac band of Gr mostly contributes to the integration when the 1T-TaS2 is in the CCDW phase. Conversely, the contribution from 1T-TaS_2 bands predominates in the Gr/normal state 1T-TaS_2 heterostructure (see Note S9, Supporting Information, for details). Such a feature implies that the source of the interfacial SHE shifts from the 1T-TaS_2 side to the Gr side following the transition from the NCCDW to the CCDW phase. In the normal state, the conventional component σ^z_{xy} shows a much larger value compared to the unconventional components σ^x_{xy} and σ^y_{xy}. However, its contribution to the CSI output should be limited because most of the current flows in the bulk 1T-TaS_2. In the CCDW state, σ^z_{xy} is smaller than that in the normal state. In this case, the current redistributes and passes predominantly through the Gr side due to the enhanced resistance of CCDW 1T-TaS_2, indicating that the CSI output should increase. These properties are consistent with $\Delta R^{S_z}_{CSI}$ observed in Device 2 (Figure 3), suggesting that the CSI induced by S_z-spin current is due to the conventional interfacial SHE. Note that unconventional σ^x_{xy} and σ^y_{xy} are comparable to σ^z_{xy} in the CCDW state, indicating that they can contribute to $R^{S_x}_{CSI}$ and $R^{S_y}_{CSI}$, respectively. However, the finite σ^y_{xy} is inconsistent with the vanishing $R^{S_y}_{CSI}$ in our experiment.

Finally, we consider the REE as the source of our observed CSI. On the one hand, the conventional REE can contribute to $R^{S_x}_{CSI}$ in our setup. On the other hand, recent studies have revealed that $R^{S_y}_{CSI}$ in Gr/TMDC van der Waals heterostructures with a twist angle[26,27] is related to an unconventional REE (UREE) induced by radial spin textures in the Rashba bands due to the lack of a mirror plane.[29–32] Indeed, we observed a radial spin texture in both Gr/CCDW 1T-TaS_2 and Gr/normal 1T-TaS_2 heterostructures (**Figures** 5 and S17 in Note S9, Supporting Information) in our calculations. Since UREE can contribute to $R^{S_y}_{CSI}$, it is reasonable to expect a non-zero $R^{S_y}_{CSI}$ in both normal and CCDW 1T-TaS_2

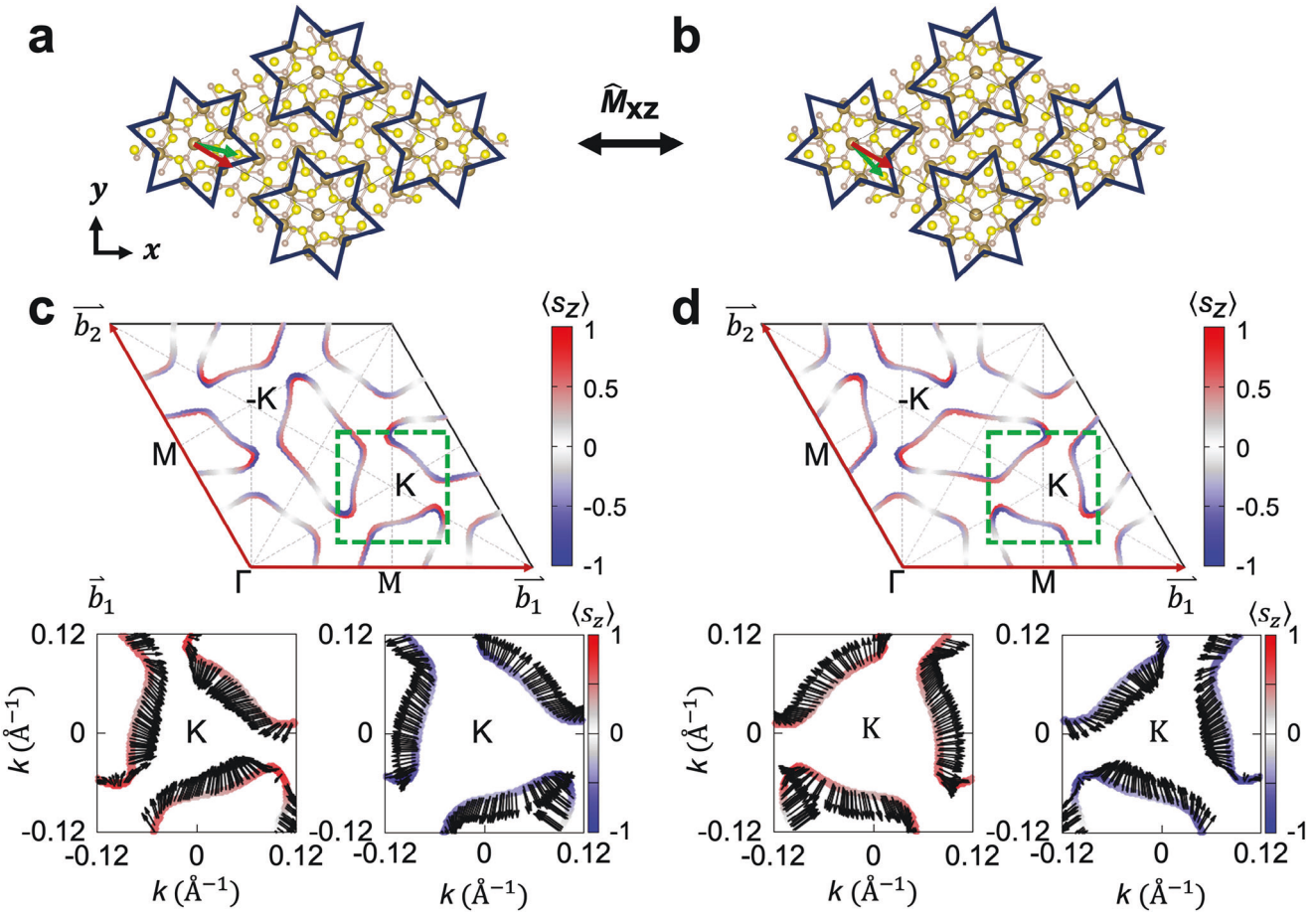

Figure 5. First-principles calculations for Rashba spin texture in Gr/1T-TaS_2 heterostructures. a,b) Two possible chiral states of Gr/CCDW 1T-TaS_2 heterostructures with opposite handedness. The green and red arrows indicate the unit vector of normal and CCDW 1T-TaS_2, respectively, which have either +13.9° or −13.9° rotation angle. They are mirror symmetric corresponding to the $\hat{M}_{xz}$ mirror operator. c,d) Handedness-dependent spin-resolved Fermi surfaces and Rashba spin textures of proximitized Dirac bands. Red and blue colors indicate out-of-plane spin components. The lower two panels show in-plane spin textures of inner (left) and outer (right) Rashba bands, near the K point (highlighted by a green box). Only the radial spin components are opposite in the chiral structures with opposite handedness.

states. This result, as in the case of the finite interfacial σ^{y}_{xy}, also contradicts our experimental observation.

To reconcile the theory with experimental observations, we examine the role of chirality in the Gr/CCDW 1T-TaS_2 heterostructures, as described in Figure 5a,b. It is well known that the lattice vectors of CCDW 1T-TaS_2 are rotated by either +13.9° or −13.9° from normal 1T-TaS_2, resulting in two helical states with opposite handedness.[40] These helical states are mirror-symmetric with respect to any mirror plane perpendicular to the TaS_2 layer and can be simultaneously observed in a single 1T-TaS_2 flake.[40] Note that this helical domain is intrinsic and is only described by mirroring, not by rotation, and is distinct from a trivial polycrystalline domain. In the presence of the Gr/CCDW 1T-TaS_2 interface, the iinversion symmetry is broken. This leads to the transformation of the helicity of 1T-TaS_2 into the chirality of the resulting heterostructures. In general, arbitrary twist angles between Gr and 1T-TaS_2 may break the mirror relation between two chiral heterostructures. However, to better grasp the underlying physics, we focused on simple examples that exhibit the mirror relation between two chiral heterostructures, ($\hat{M}_{xz}$, in our case) and investigated the role of chiral domains.

We present the spin-resolved Fermi surfaces of both chiral heterostructures in Figure 5c,d. Near the K point (indicated by a green box), we observed a Gr Dirac band with distinct spin splitting, resulting in inner (red) and outer (blue) Rashba bands. The in-plane spin textures of both Rashba bands are shown in the lower two panels. Our results reveal opposite radial spin textures for different handedness, while the conventional Rashba component remains the same in both chiral states, which means that the radial spin is locked to the chirality[42–45] (see Figures S18 and S19, Supporting Information, for more details). This is because the $\hat{M}_{xz}$ operation flips S_x, S_z, and k_y, but not S_y and k_x. Here k_x (k_y) represents the momentum along the $x(y)$-axis. These results imply that conventional REE is preserved whereas UREE should disappear when both chiral CDW structures coexist. The effect of the chiral domain on the interfacial SHE can also be deduced from the quantity $S^{k}_{ij} = \nu_i S_k \nu_j$, where ν represents the velocity of electrons.[43] This quantity has the same symmetry as Ω^{k}_{ij}.

Similar to UREE, $\hat{M}_{xz}\Omega^{y}_{xy} = \nu_x S_y(-\nu_y) = -\Omega^{y}_{xy}$, indicating that the total interfacial σ^{y}_{xy} is also canceled out if the two handedness coexist. We have conducted additional calculations on the Gr/CCDW 1T-TaS_2 heterostructure with a twisted angle of 5.2°. The results show that the radial spin textures are consistently opposite in the two structures with reversed handedness (Figure S20, Supporting Information), evidencing the robustness of the observed cancellation.

Note that the CDW domains in the NCCDW phase of 1T-TaS_2 exhibit an average size of ≈10 nm at 200 K.[46,47] The chiral domain expands and merges during the NCCDW-CCDW phase transition, which can increase its size in the CCDW phase. However, this scale is much smaller than our micrometer-level devices. Although nanometer- and millimeter-size chiral domains have been reported in recent studies,[36,48,49] the size could also be restricted by the appearance of impurities.[40] Therefore, we deduce that the contributions from UREE and interfacial σ^{y}_{xy} are canceled out due to the mixed chiral domains with opposite handedness, that is, the vanishing $R^{S_y}_{CSI}$ in our experiments, whereas the conventional REE and interfacial σ^{x}_{xy} contribute to the observed $R^{S_x}_{CSI}$. Hence, it can be concluded that the intrinsic chirality of the CCDW phase governs the evolution of both UREE and the interfacial unconventional SHE. An alternative hypothesis, for instance, a non-uniform current distribution along the *x*-axis arising from the high-conductivity normal-phase channels in between the commensurate star-of-David domains of the NCCDW phase, could potentially generate the $R^{S_y}_{CSI}$ component by the conventional SHE. However, we maintain a net zero current along the *x*-axis during the measurements, ruling out this scenario as the origin of the unconventional CSI.

In combination with the control of the commensurability[34,35] and the helicity[36] of the CDW phase in 1T-TaS_2 achieved via electrical stimulation, our observation provides new opportunities for designing functional electric-field-control-of spintronic devices with a degree of freedom from the TMDC material itself. For instance, the tunable CSI could be exploited in spin-orbit torque memory devices, where only specific unconventional CSI components contribute to the deterministic switching of perpendicular magnetization. This process has been demonstrated in low-symmetry materials,[50–53] where the underlying symmetry of CSI phenomena, and the allowed charge-spin response tensor, are governed by the crystal symmetry.[43,54] The present 1T-TaS_2, with tunable CDW between high and low symmetry crystalline phases, simplifies such geometric obstacles and offers an enticing platform for realizing such on-demand switchable CSI.

3. Conclusion

In summary, we report the first demonstration of tunable CSI in Gr/1T-TaS_2 van der Waals heterostructures exploiting the phase transition of the CDW in the TMDC. We observe omnidirectional CSI (i.e., with spins oriented in all three directions) in the heterostructures when the CDW in 1T-TaS_2 does not show commensurability. Whereas the CSI components induced by S_x- and S_z-polarized spin currents are enhanced after a phase transition to a commensurate state, the one induced by S_y-polarized spin currents are switched off. By comparing our experimental results with first-principles calculations, we conclude that the disappearance of this CSI component is due to the appearance of chiral CDW multidomains. Our findings provide insights into the interplay between proximity, commensurability, and chirality of the CDW in the Gr/1T-TaS_2 system and establish it as a platform for low-dimensional functional spin-orbitronic devices.

4. Experimental Section

Device Fabrication: The graphene/1T-TaS_2 heterostructures were assembled by the dry viscoelastic transfer technique. Elongated graphene flakes were first exfoliated from highly oriented pyrolytic graphite (provided by NGS Naturegraphit GmBH) and deposited on highly n-type doped Si substrates with a 300-nm-thick SiO_2 layer. The monolayer and bilayer graphene flakes were distinguished based on the contrast using an optical microscope and confirmed by Raman spectroscopy. The 1T-TaS_2 flakes were exfoliated from a single crystal provided by 2D Semiconductors (Device 1) and by HQ Graphene (Devices 2 and 3) onto a piece of polydimethylsiloxane (PDMS). After identifying strips with suitable width and thickness (confirmed later by an atomic force microscopy) using an optical microscope, the 1T-TaS_2 flakes were then transferred from the PDMS stamp to the SiO_2/Si substrate, where they formed Hall bar cross junctions with the elongated graphene flakes. The exfoliation of 1T-TaS_2 flakes and transfer processes were carried out in a glovebox with an Ar atmosphere. Non-magnetic Pd (5 nm)/Au (45 nm) electrodes were used to contact the graphene and 1T-TaS_2 and fabricated using the standard processes of e-beam lithography, evaporation, and lift-off. TiO_x/Co/Au FM electrodes were deposited on the graphene flake to inject/detect the spin current and fabricated using the same processes as Pd/Au electrodes. During the evaporation process, ~0.3 nm of Ti was first deposited, followed by a 10-min ambient oxidization process that formed the TiO_x layer. Then, 35 nm of Co and 15 nm of Au were evaporated. The 15-nm-thick Au layer was a capping layer to protect the Co layer from oxidization. The width of FM electrodes was either 150 or 350 nm to give different shape anisotropies.

Electrical Measurements: Local and non-local magnetotransport measurements were performed in a physical property measurement system (PPMS) by Quantum Design, where the temperature was varied and magnetic fields were applied in different directions. The measurements were carried out using a dc reversal technique with a Keithley 2182 nanovoltmeter and a 6221 current source. A back-gate voltage was applied to the highly n-type doped Si substrate using a Keithley 2636B source meter unit to adjust the Fermi level of the graphene.

Separation of the Different CSI Components: In CSI measurements, the spin polarization (S) of the spin current (j_s) diffusing in graphene is controllable by a magnetic field. By applying an external magnetic field along the *x*-axis (H_x) or *z*-axis (H_z), which respectively correspond to the in-plane and out-of-plane hard axes of the FM electrode, the spin in the spin current undergoes precession in the *y*-*z* or *x*-*y* plane. These precessions give additional spin-polarization components in the spin current. The magnetization $\boldsymbol{M}$ of the FM electrode is also pulled by the external magnetic field. The amplitude of different CSI components ($\Delta R^{S_i}_{CSI}$) is thus proportional to the projection of $\boldsymbol{M}$ along the corresponding spin polarization direction (S_i) of the spin current. To distinguish the components induced by a spin current with different polarizations, the non-local CSI resistance R_{NL} is measured as a function of H_x or H_z.

By scanning H_x, the R_{NL} component induced by S_x ($R^{S_x}_{CSI}$) is zero when $H_x = 0$ because the initial $\boldsymbol{M}$ is perpendicular to S_x. The value of $R^{S_x}_{CSI}$ increases as H_x increases and finally saturates when $\boldsymbol{M}$ is fully aligned along the *x*-axis. This yields an *S*-shaped curve similar to the conventional SHE in metals[41] or the REE in 2D systems.[21] $R^{S_x}_{CSI}$ is unaffected by the initial direction of $\boldsymbol{M}$ (+*y* or −*y*) as its value is only determined by the projection of $\boldsymbol{M}$ along the *x*-axis. On the other hand, because the spin current precesses within the *y*-*z* plane under a small H_x, the R_{NL} components originating from S_y ($R^{S_y}_{CSI}$) and S_z ($R^{S_z}_{CSI}$) show a spin precession feature as a function of H_x. Considering the initial $\boldsymbol{M}$ along the *y*-axis, the precession of $R^{S_y}_{CSI}$ and

$R_{CSI}^{S_z}$ should show symmetric and antisymmetric line shapes, respectively, as reported in other Gr/TMDC heterostructures.[20–22,24,26,27] The signs of $R_{CSI}^{S_y}$ and $R_{CSI}^{S_z}$ reverse after switching the initial direction of $\boldsymbol{M}$ because the initial projections of $\boldsymbol{M}$ onto the *y*-axis are opposite. Both $R_{CSI}^{S_y}$ and $R_{CSI}^{S_z}$ will decrease to zero at high H_x due to the *x*-axis pulling of $\boldsymbol{M}$ and the spin dephasing. Based on these properties, $R_{CSI}^{S_x}$, $R_{CSI}^{S_y}$, and $R_{CSI}^{S_z}$ can be separated by measuring R_{NL} with the initial direction of $\boldsymbol{M}$ set along the $+y$ ($R_{NL}^{\uparrow}$) and $-y$ ($R_{NL}^{\downarrow}$) directions. $R_{CSI}^{S_x}$ can be extracted by taking their average ($R_{NL}^{avg}(H_x) = (R_{NL}^{\uparrow} + R_{NL}^{\downarrow})/2$), since the sign of $R_{NL}^{S_x}$ is the same in both cases. The contribution of $R_{CSI}^{S_x}$ can be removed by taking half of the difference ($R_{NL}^{diff}(H_x) = (R_{NL}^{\uparrow} - R_{NL}^{\downarrow})/2$), where the $R_{CSI}^{S_y}$ and $R_{CSI}^{S_z}$ contributions remain because their signs are opposite after reversing the initial direction of $\boldsymbol{M}$. $R_{CSI}^{S_y}$ and $R_{CSI}^{S_z}$ can be further separated by symmetrizing and antisymmetrizing $R_{NL}^{diff}(H_x)$, respectively, due to their different precession features.

The line shapes of R_{NL} measured under H_z are similar. In this case, the spin current precesses in the *x*-*y* plane under a small H_z. $R_{CSI}^{S_y}$ and $R_{CSI}^{S_x}$ are symmetric and antisymmetric against H_z. Their signs reverse after switching the initial direction of $\boldsymbol{M}$. Therefore, $R_{CSI}^{S_y}$ and $R_{CSI}^{S_x}$ can be separated by symmetrizing and antisymmetrizing $R_{NL}^{diff}(H_z)$ when H_z is scanned. Although $R_{CSI}^{S_z}$ versus H_z should have an *S*-shaped curve, similar to $R_{CSI}^{S_x}$ measured versus H_x, a linear background exists in R_{NL} because of the large ordinary Hall effect in Gr. Hence, it is difficult to determine $R_{CSI}^{S_z}$ using an H_z-dependent measurement.

First-Principles Calculations: We performed first-principles calculations based on DFT[55] as implemented in the Quantum Espresso package.[56,57] The exchange-correlation functional was treated within the generalized gradient approximation of Perdew–Burke–Ernzerhof (PBE).[58] The kinetic energy cutoff of electronic wavefunctions and charge density were chosen to be 80 and 640 Ry, respectively. To mimic the 2D layered heterostructure, a large vacuum region was included in periodic cells, and used Grimme-D3 van der Waals correction[59] where necessary. The spin-orbit coupling was included in the electronic structure calculations. The k-grid meshes were chosen to be $15 \times 15 \times 9$, $5 \times 5 \times 9$, and $4 \times 4 \times 1$ for bulk normal 1T-TaS_2, bulk CCDW 1T-TaS_2, and graphene/1T-TaS_2 heterostructures, respectively.

The intrinsic spin Hall conductivity $\sigma_{\alpha\beta}^{\gamma}$ was calculated by the Kubo–Greenwood formula as[60]

$$\sigma_{\alpha\beta}^{\gamma}(\varepsilon) = \frac{\hbar}{\Omega_C N_k} \sum_{\boldsymbol{k}} \sum_{n} f_{n\boldsymbol{k}} \sum_{m \neq n} \frac{2\mathrm{Im}\left[\left\langle n\boldsymbol{k}\middle|\hat{j}_{\alpha}^{\gamma}\middle|m\boldsymbol{k}\right\rangle \left\langle m\boldsymbol{k}\middle|-e\hat{v}_{\beta}\middle|n\boldsymbol{k}\right\rangle\right]}{\left(\varepsilon_{n\boldsymbol{k}} - \varepsilon_{m\boldsymbol{k}}\right)^2 + \eta^2} \quad (1)$$

where Ω_C and N_k indicate the cell volume and the number of k-points used for k-space sampling, $f_{n\boldsymbol{k}}$ indicates Fermi-Dirac distribution, $\hat{j}_{\alpha}^{\gamma}$ is the spin current operator defined as $\hat{j}_{\alpha}^{\gamma} = \frac{1}{2}\{\hat{s}^{\gamma}, \hat{v}_{\alpha}\}$, and $\hat{s}^{\gamma}$ and $\hat{v}_{\alpha,\beta}$ are spin and velocity operators, respectively. η is an adjustable smearing parameter. The numerical calculations were performed by the Wannier90 package.[61–64] For wannierization, *d*, *p*, and p_z orbital projections were used for Ta, S, and C atoms, and additional sp^2 orbital projections were alternatively added to the C atoms. To obtain the converged results, a fine k-mesh grid of $300 \times 300 \times 180$, $80 \times 80 \times 160$, and $600 \times 600 \times 1$ were used for normal 1T-TaS_2, CCDW 1T-TaS_2, and graphene/1T-TaS_2 heterostructure, respectively. The corresponding broadening constant of η was chosen to be 10 meV. In the graphene/1T-TaS_2 heterostructure, an effective thickness of 9.46 Å was used in evaluating its $\sigma_{\alpha\beta}^{\gamma}$ in the unit of $((\hbar/e)S/\mathrm{cm})$ (presented in Table 1).

Supporting Information

Supporting Information is available from the Wiley Online Library or from the author.

Acknowledgements

The authors thank F. de Juan and H. Ochoa for the fruitful discussions. The authors acknowledge funding by the "Valleytronics" Intel Science Technology Center, the Spanish MCIN/AEI and by ERDF "A way of making Europe" (Project No. PID2021-122511OB-I00 and "Maria de Maeztu" Units of Excellent Programme No. CEX2020-001038-M), the European Union H2020 under the Marie Sklodowska-Curie Actions (Project Nos. 0766025-QuESTech and 955671-SPEAR), and Diputación de Gipuzkoa (Project No. 2021-CIEN-000037-01). S.L. and T.L. were partially supported by the National Science Foundation through the University of Minnesota MRSEC under Award Number DMR-2011401. Z.C. and J.I.-A. acknowledge postdoctoral fellowship support from the "Juan de la Cierva" Programme by the Spanish MCIN/AEI (grants No. FJC2021-047257-I and FJC2018-038688-I, respectively). S.L. was also supported by the Basic Science Research Program through the National Research Foundation of Korea (NRF) funded by the Ministry of Education (NRF-2021R1A6A3A14038837). N.O. thanks the Spanish MCIN/AEI for support from a Ph.D. fellowship (Grant No. BES-2017-07963). B.M.-G. thanks support from the "Ramón y Cajal" Programme by the Spanish MCIN/AEI (grant no. RYC2021-034836-I).

Conflict of Interest

The authors declare no conflict of interest.

Author Contributions

Z.C., S.L., and H.Y. contributed equally to this work. Z.C. and F.C. conceived this study. Z.C. fabricated and characterized the devices, performed the electrical measurements, and analyzed the data with the help of H.Y., E.D., C.K.S, J.I.-A., F.H., and N.O. S.L. and T.L. performed the first-principles calculations. All authors contributed to the discussion on the results. Z.C., S.L., and F.C. wrote the manuscript with input from all authors.

Data Availability Statement

The data that support the findings of this study are available from the corresponding author upon reasonable request.

Keywords

charge density wave, charge-spin interconversion, chirality, graphene, van der Waals heterostructures

Received: October 16, 2023
Revised: December 10, 2023
Published online: January 26, 2024

[1] K. Garello, F. Q. Yasin, S. Couet, L. Souriau, J. Swerts, S. Rao, S. Van Beek, W. Kim, Y. Liu, S. Kundu, D. Tsvetanova, K. Croes, N. Jossart, E. Grimaldi, M. Baumgartner, D. Crotti, A. Fumémont, P. Gambardella, G. S. Kar, in *2018 IEEE Symp. on VLSI Circuits*, IEEE, Piscataway, NJ **2018**, pp. 81–82.

[2] S. Manipatruni, D. E. Nikonov, C.-C. Lin, T. A. Gosavi, H. Liu, B. Prasad, Y.-L. Huang, E. Bonturim, R. Ramesh, I. A. Young, *Nature* **2019**, *565*, 35.
[3] V. T. Pham, I. Groen, S. Manipatruni, W. Y. Choi, D. E. Nikonov, E. Sagasta, C.-C. Lin, T. A. Gosavi, A. Marty, L. E. Hueso, I. A. Young, F. Casanova, *Nat. Electron.* **2020**, *3*, 309.
[4] J. Sinova, S. O. Valenzuela, J. Wunderlich, C. H. Back, T. Jungwirth, *Rev. Mod. Phys.* **2015**, *87*, 1213.
[5] A. Manchon, H. C. Koo, J. Nitta, S. M. Frolov, R. A. Duine, *Nat. Mater.* **2015**, *14*, 871.
[6] T. Kimura, Y. Otani, T. Sato, S. Takahashi, S. Maekawa, *Phys. Rev. Lett.* **2007**, *98*, 156601.
[7] C. Sanz-Fernández, V. T. Pham, E. Sagasta, L. E. Hueso, I. V. Tokatly, F. Casanova, F. S. Bergeret, *Appl. Phys. Lett.* **2020**, *117*, 142405.
[8] I. M. Miron, K. Garello, G. Gaudin, P.-J. Zermatten, M. V. Costache, S. Auffret, S. Bandiera, B. Rodmacq, A. Schuhl, P. Gambardella, *Nature* **2011**, *476*, 189.
[9] L. Liu, C.-F. Pai, Y. Li, H. W. Tseng, D. C. Ralph, R. A. Buhrman, *Science* **2012**, *336*, 555.
[10] A. R. Mellnik, J. S. Lee, A. Richardella, J. L. Grab, P. J. Mintun, M. H. Fischer, A. Vaezi, A. Manchon, E.-A. Kim, N. Samarth, D. C. Ralph, *Nature* **2014**, *511*, 449.
[11] Y. Fan, P. Upadhyaya, X. Kou, M. Lang, S. Takei, Z. Wang, J. Tang, L. He, L.-T. Chang, M. Montazeri, G. Yu, W. Jiang, T. Nie, R. N. Schwartz, Y. Tserkovnyak, K. L. Wang, *Nat. Mater.* **2014**, *13*, 699.
[12] A. Avsar, H. Ochoa, F. Guinea, B. Özyilmaz, B. J. van Wees, I. J. Vera-Marun, *Rev. Mod. Phys.* **2020**, *92*, 021003.
[13] W. Han, R. K. Kawakami, M. Gmitra, J. Fabian, *Nat. Nanotechnol.* **2014**, *9*, 794.
[14] A. K. Geim, I. V. Grigorieva, *Nature* **2013**, *499*, 419.
[15] J. F. Sierra, J. Fabian, R. K. Kawakami, S. Roche, S. O. Valenzuela, *Nat. Nanotechnol.* **2021**, *16*, 856.
[16] J. H. Garcia, A. W. Cummings, S. Roche, *Nano Lett.* **2017**, *17*, 5078.
[17] M. Milletarì, M. Offidani, A. Ferreira, R. Raimondi, *Phys. Rev. Lett.* **2017**, *119*, 246801.
[18] J. H. Garcia, M. Vila, A. W. Cummings, S. Roche, *Chem. Soc. Rev.* **2018**, *47*, 3359.
[19] M. Offidani, M. Milletarì, R. Raimondi, A. Ferreira, *Phys. Rev. Lett.* **2017**, *119*, 196801.
[20] C. K. Safeer, J. Ingla-Aynés, F. Herling, J. H. Garcia, M. Vila, N. Ontoso, M. R Calvo, S. Roche, L. E. Hueso, F. Casanova, *Nano Lett.* **2019**, *19*, 1074.
[21] L. A. Benítez, W. Savero Torres, J. F. Sierra, M. Timmermans, J. H. Garcia, S. Roche, M. V. Costache, S. O. Valenzuela, *Nat. Mater.* **2020**, *19*, 170.
[22] F. Herling, C. K. Safeer, J. Ingla-Aynés, N. Ontoso, L. E. Hueso, F. Casanova, *APL Mater.* **2020**, *8*, 071103.
[23] T. S. Ghiasi, A. A. Kaverzin, J. Blah, B. J. van Wees, *Nano Lett.* **2019**, *19*, 5959.
[24] C. K. Safeer, N. Ontoso, J. Ingla-Aynés, F. Herling, V. T. Pham, A. Kurzmann, K. Ensslin, A. Chuvilin, I. Robredo, M. G. Vergniory, F. de Juan, L. E. Hueso, M. Reyes Calvo, F. Casanova, *Nano Lett.* **2019**, *19*, 8758.
[25] B. Zhao, B. Karpiak, D. Khokhriakov, A. Johansson, A. Md Hoque, X. Xu, Y. Jiang, I. Mertig, S. Dash, *Adv. Mater.* **2020**, *32*, 2000818.
[26] L. Camosi, J. Světlík, M. V. Costache, W. Savero Torres, I. Fernández Aguirre, V. Marinova, D. Dimitrov, M. Gospodinov, J. F. Sierra, S. O. Valenzuela, *2D Mater.* **2022**, *9*, 035014.
[27] J. Ingla-Aynés, I. Groen, F. Herling, N. Ontoso, C. K. Safeer, F. de Juan, L. E. Hueso, M. Gobbi, F. Casanova, *2D Mater.* **2022**, *9*, 045001.
[28] N. Ontoso, C. K. Safeer, F. Herling, J. Ingla-Aynés, H. Yang, Z. Chi, B. Martin-Garcia, I. Robredo, M. G. Vergniory, F. de Juan, M. R Calvo, L. E. Hueso, F. Casanova, *Phys. Rev. Appl.* **2023**, *19*, 014053.
[29] T. Naimer, K. Zollner, M. Gmitra, J. Fabian, *Phys. Rev. B* **2021**, *104*, 195156.
[30] A. Veneri, D. T. S. Perkins, C. G. Péterfalvi, A. Ferreira, *Phys. Rev. B* **2022**, *106*, L081406.
[31] S. Lee, D. J. de Sousa, Y.-K. Kwon, F. de Juan, Z. Chi, F. Casanova, T. Low, *Phys. Rev. B* **2022**, *106*, 165420.
[32] K. Szałowski, M. Milivojevic, D. Kochan, M. Gmitra, *2D Mater.* **2023**, *10*, 025013.
[33] R. Comin, A. Damascelli, *Annu. Rev. Condens. Matter Phys.* **2016**, *7*, 369.
[34] M. Yoshida, Y. Zhang, J. Ye, R. Suzuki, Y. Imai, S. Kimura, A. Fujiwara, Y. Iwasa, *Sci. Rep.* **2014**, *4*, 7302.
[35] Y. Ma, D. Wu, C. Lu, C. Petrovic, *Appl. Phys. Lett.* **2020**, *116*, 171906.
[36] G. Liu, T. Qiu, K. He, Y. Liu, D. Lin, Z. Ma, Z. Huang, W. Tang, J. Xu, K. Watanabe, T. Taniguchi, L. Gao, J. Wen, J.-M. Liu, B. Yan, X. Xi, *Nat. Nanotechnol.* **2023**, *18*, 854.
[37] F. Zwick, H. Berger, I. Vobornik, G. Margaritondo, L. Forró, C. Beeli, M. Onellion, G. Panaccione, A. Taleb-Ibrahim, M. Grioni, *Phys. Rev. Lett.* **1998**, *81*, 1058.
[38] D. Cho, G. Gye, J. Lee, S.-H. Lee, L. Wang, S.-W. Cheong, H. W. Yeom, *Nat. Commun.* **2017**, *8*, 392.
[39] Y. D. Wang, W. L. Yao, Z. M. Xin, T. T. Han, Z. G. Wang, L. Chen, C. Cai, Y. Li, Y. Zhang, *Nat. Commun.* **2020**, *11*, 4215.
[40] H. F. Yang, K. Y. He, J. Koo, S. W. Shen, S. H. Zhang, G. Liu, Y. Z. Liu, C. Chen, A. J. Liang, L. Huang, M. X. Wang, J. J. Gao, X. Luo, L. X. Yang, J. Liu, Y. Sun, S. C. Yan, B. H. Yan, Y. L. Chen, X. Xi, Z. K. Liu, *Phys. Rev. Lett.* **2022**, *129*, 156401.
[41] W. Yan, E. Sagasta, M. Ribeiro, Y. Niimi, L. E. Hueso, F. Casanova, *Nat. Commun.* **2017**, *8*, 661.
[42] C. K. Safeer, F. Herling, W. Y. Choi, N. Ontoso, J. Ingla-Aynés, L. E. Hueso, F. Casanova, *2D Mater.* **2021**, *9*, 015024.
[43] A. Roy, M. H. D. Guimarães, J. Sławińska, *Phys. Rev. Mater.* **2022**, *6*, 045004.
[44] M. Hirayama, R. Okugaw, S. Murakami, T. Miyake, *Phys. Rev. Lett.* **2015**, *114*, 206401.
[45] M. Sakano, M. Hirayama, T. Takahashi, S. Akebi, M. Nakayama, K. Kuroda, K. Taguchi, T. Yoshikawa, K. Miyamoto, T. Okuda, K. Ono, H. Kumigashira, T. Ideue, Y. Iwasa, N. Mitsuishi, K. Ishizaka, S. Shin, T. Miyake, S. Murakami, T. Sasagawa, T. Konda, *Phys. Rev. Lett.* **2020**, *124*, 136404.
[46] X. L. Wu, C. M. Lieber, *Phys. Rev. Lett.* **1990**, *64*, 1150.
[47] R. Thomson, B. Burk, A. Zettl, J. Clarke, *Phys. Rev. B* **1994**, *49*, 16899.
[48] Y. Zhao, Z. Nie, H. Hong, X. Qiu, S. Han, Y. Yu, M. Liu, X. Qiu, K. Liu, S. Meng, L. Tong, J. Zhang, *Nat. Commun.* **2023**, *14*, 2223.
[49] J. W. Park, G. Y. Cho, J. Lee, H. W. Yeom, *Nat. Commun.* **2019**, *10*, 4038.
[50] D. MacNeill, G. M. Stiehl, M. H. D. Guimarães, R. A. Buhrman, J. Park, D. C. Ralph, *Nat. Phys.* **2017**, *13*, 300.
[51] I.-H. Kao, R. Muzzio, H. Zhang, M. Zhu, J. Gobbo, S. Yuan, D. Weber, R. Rao, J. Li, J. H. Edgar, J. E. Goldberger, J. Yan, D. G. Mandrus, J. Hwang, R. Cheng, J. Katoch, S. Singh, *Nat. Mater.* **2022**, *21*, 1029.
[52] D. D. Sousa, Haney, J. Wang, A. T. Low, *Phys. Rev. Appl.* **2022**, *18*, 054020.
[53] L. Liu, C. Zhou, X. Shu, C. Li, T. Zhao, W. Lin, J. Deng, Q. Xie, S. Chen, J. Zhou, R. Guo, H. Wang, J. Yu, S. Shi, Yang, S. Pennycook, A. Manchon, J. Chen, *Nat. Nanotechnol.* **2021**, *15*, 277.
[54] D. Culcer, R. Winkler, *Phys. Rev. Lett.* **2007**, *99*, 226601.
[55] W. Khon, L. J. Sham, *Phys. Rev.* **1965**, *140*, A1133.
[56] P. Giannozzi, S. Baroni, N. Bonini, M. Calandra, R. Car, C. Cavazzoni, D. Ceresoli, G. L. Chiarotti, M. Cococcioni, I. Dabo, A. D. Corso, S. de Gironcoli, S. Fabris, G. Fratesi, R. Gebauer, U. Gerstmann,

C. Gougoussis, A. Kokalj, M. Lazzeri, L. Martin-Samos, N. Marzari, F. Mauri, R. Mazzarello, S. Paolini, A. Pasquarello, L. Paulatto, C. Sbraccia, S. Scandolo, G. Sclauzero, A. P. Seitsonen, et al., *J. Phys.: Condens. Matter* **2009**, *21*, 395502.

[57] P. Giannozzi, O. Andreussi, T. Brumme, O. Bunau, M. B. Nardelli, M. Calandra, R. Car, C. Cavazzoni, D. Ceresoli, M. Cococcioni, N. Colonna, I. Carnimeo, A. D. Corso, S. de Gironcoli, P. Delugas, R. A. DiStasio Jr, A. Ferretti, A. Floris, G. Fratesi, G. Fugallo, R. Gebauer, U. Gerstmann, F. Giustino, T. Gorni, J. Jia, M. Kawamura, H.-Y. Ko, A. Kokalj, E. Küçükbenli, M. Lazzeri, et al., *J. Phys.: Condens. Matter* **2017**, *29*, 465901.

[58] J. Perdew, K. Burke, M. Ernzerhof, *Phys. Rev. Lett.* **1996**, *77*, 3865.

[59] S. Grimme, *J. Comput. Chem.* **2006**, *27*, 1787.

[60] G. Y. Guo, S. Murakami, T.-W. Chen, N. Nagaosa, *Phys. Rev. Lett.* **2008**, *100*, 096401.

[61] A A. Mostofi, J R. Yates, G. Pizzi, Y-Su Lee, I. Souza, D. Vanderbilt, N. Marzari, *Comput. Phys. Commun.* **2017**, *185*, 2309.

[62] G. Pizzi, V. Vitale, R. Arita, S. Blügel, F. Freimuth, G. Géranton, M. Gibertini, D. Gresch, C. Johnson, T. Koretsune, J. Ibañez-Azpiroz, H. Lee, J.-M. Lihm, D. Marchand, A. Marrazzo, Y. Mokrousov, J. I. Mustafa, Y. Nohara, Y. Nomura, L. Paulatto, S. Poncé, T. Ponweiser, J. Qiao, F. Thöle, S. S. Tsirkin, M. Wierzbowska, N. Marzari, D. Vanderbilt, I. Souza, A. A. Mostofi, et al., *J. Phys.: Condens. Matter* **2020**, *32*, 165902.

[63] I. Souza, N. Marzari, D. Vanderbilt, *Phys. Rev. B* **2001**, *65*, 035109.

[64] J. Qiao, J. Zhou, Z. Yuan, W. Zhao, *Phys. Rev. B* **2018**, *98*, 214402.